Surface reconstructions and modified surface states in La_{1−x}Ca_{x}MnO_{3}

Rama K. Vasudevan, Hemant Dixit, Alexander Tselev, Liang Qiao, Tricia L. Meyer, Valentino R. Cooper, Arthur P. Baddorf, Ho Nyung Lee, P. Ganesh, and Sergei V. Kalinin

Phys. Rev. Materials **2**, 104418 — Published 31 October 2018

DOI: 10.1103/PhysRevMaterials.2.104418

To be resubmitted to Phys. Rev. Mat.

Surface reconstructions and modified surface states in $La_{1-x}Ca_xMnO_3$

Rama K. Vasudevan[1,2,□], Hemant Dixit[3, □], Alexander Tselev[4], Liang Qiao[1,5], Tricia Meyer[3], Valentino R. Cooper[3], Arthur P. Baddorf[1,2], Ho Nyung Lee[3], P. Ganesh[1,2,*] and Sergei V. Kalinin[1,2,**]

[1]Center for Nanophase Materials Sciences, [2]ORNL Institute for Functional Imaging of Materials, and [3]Materials Science and Technology Division, Oak Ridge National Laboratory, Oak Ridge, TN 37831, USA

[4]Department of Physics and CICECO–Aveiro Institute of Materials, University of Aveiro, 3810-193 Aveiro, Portugal

[5]Present Address: School of Materials, The University of Manchester, Manchester, M13 9PL, UK

Abstract

The unique functionalities present at surfaces and interfaces of complex oxides have attracted intense research in the past decade. Yet, the fundamental mechanisms underpinning functionality are often elusive, especially in doped manganites, limiting their implementation in functional electronic devices such as memristors and spin valves. Here, we present a local probe-based study on mixed-terminated $La_{5/8}Ca_{3/8}MnO_3$ (LCMO) films, and reveal surface metallicity in a thin-film grown by pulsed laser deposition. Using first-principles density functional theory calculations with Hubbard correction that are more accurate to capture effects of correlation in these systems, we show that for Ca-segregated (001) LCMO surfaces the (La,Ca)O-site terminated surfaces are half-metallic due to delocalized Mn-*d* states populating the Fermi Level, whereas the MnO_2-site terminated surfaces exhibit a half-metallic or insulating character depending on the type of surface reconstruction. Computations not only explain the current measurements, but also explain other recent surface measurements on LCMO thin-films, leading to a coherent picture of how the crucial link between surface segregation and Jahn-Teller couplings in the manganese oxides tune the surface electronic/magnetic structure, thereby pointing to the fine control of transport and magnetism at the conductive oxide surface independent of the bulk.

Keywords: Manganite, Surface, Metallicity, DFT, Metal-Insulator transitions

*ganeshp@ornl.gov, **sergei2@ornl.gov

□ These two authors contributed equally to this manuscript

Introduction

The unique functionalities at complex oxide surfaces and interfaces, ranging from ferromagnetic domain walls in an antiferromagnetic material,[1] to conduction at the interface between two band insulators,[2] has received significant attention in light of potential applications as next-generation electronic and memory devices.[3] However, the fundamental mechanisms underpinning the unique functionality are often elusive and are vigorously debated.[4] This is especially true of the manganese oxides (manganites),[5] which display a rich tapestry of phases as a result of interplay between their chemistry and spin, charge, lattice and orbital degrees of freedom[6] with strong electronic correlations, that make both experimental decoupling of distinct mechanisms, as well as computational *ab-initio* modelling, extremely challenging. Moreover, epitaxial thin-films, which serve as a test-bed for experimentation, introduce additional complications such as strain,[7] off-stoichiometry,[8] surface cation segregation,[9–11] changes to octahedral rotations[12] and Jahn-Teller (JT) coupling[13] that have resulted in a distinct lack of agreement in the published literature on the impact of substrates and thickness on electronic properties of the manganites.[7,14,15]

Although nanoscale complex oxides, including manganites, have been studied intensely for the past two decades, the unique functionalities that make them attractive have not resulted in commercial functional nanoelectronic devices to date, partly as a result of irreproducibility of behaviors (in addition to the need for integration on semiconducting substrates). Unlike traditional semiconductors which can be designed and optimized macroscopically through chemical doping, manganites are characterized by electronic correlations[16] combined with strong electron-phonon coupling. This highly localized nature of the electrons necessitates measurements of chemical, physical and electronic properties at the smallest (i.e., atomic) lengths scales to extricate the relevant structure-property relations. Moreover, the coupling between the various order parameters and chemical and structural

degrees of freedom (e.g., oxygen vacancy ordering[17,18]) complicate interpretation of experimental results from bulk measurements. Local probes provide a strong alternative that can potentially decouple these effects, but to date, the surfaces of manganite films have not been well studied at atomic length scales, given the difficulty in sample preparation.[19,20] Though some atomic scale studies involving fracture of perovskite films exist,[21–24] comparatively little is known about surface electronic structures of these materials. Wei *et. al.*[25] used scanning tunneling microscopy (STM) of $La_{0.7}Ca_{0.3}MnO_3$ films and observed characteristic peaks in the dI/dV spectrum that were assigned to a half-metallic behavior in the ferromagnetic phase at low temperature, although the termination of the films were not stated and atomic resolution was not achieved. Using an *in-situ* approach, Fuchigami *et. al.*[20] prepared LCMO films and showed that metallic behavior on the *B*-site (MnO_2) termination could be observed, which was argued to be due to the Mn *d*-states crossing the Fermi level, but the underlying reason behind what drives the Mn *d*-states across the Fermi level is unclear. Moreover, little is known about the *A*-site ((La,Ca)O) termination. While Ca segregation might be expected, the level of Ca segregation[26] in these films is unknown. This is a critical parameter as an increase in Ca doping at the surface modulates the JT distortions as well as the valency of the Mn atoms near the surface, that are fundamental to stabilizing long-ranged magnetic order as well as driving the metal-insulator transition in the manganites, thereby influencing the electronic/magnetic properties. If this influence is local, then a modulated Ca segregation across the film, might additionally suggest a modulated electronic/magnetic profile. Progress in this field requires improved experimental data on surface chemical composition, atomic level Scanning Tunneling Spectroscopy (STS) as a function of termination, and modelling the electronic structure of reconstructed surfaces as a function of composition – something which has thus far been lacking, both in terms of available first principles theory, as well as *in-situ* imaging and electron spectroscopy

measurements of the film surface. Almost all of the theoretical studies involve model Hamiltonians[13] and are not material/chemistry/structure specific, and thus are of limited use to make specific predictions of material properties, which is a requirement for the development and integration of manganites (and indeed, complex oxides in general) in functional electronic devices such as non-volatile memories, spin valves, and transistors.

It has been known for decades that the transport and magnetic properties of the mixed valence manganites with structure $R_{1-x}R'_xMnO_3$ (R is a rare earth, R' = Ca, Sr, Ba…) depend heavily on the structural distortions of the idealized unit cell, and in particular, the existence of Jahn-Teller distortions.[6,27–29] In the case of Mn^{3+} (e.g., for $LaMnO_3$), a $t_{2g}^3e_g^1$ arrangement is expected, but since only 2/3 of the Mn-O bonds can be covalent, by the Jahn-Teller theorem[30] the system lifts degeneracy by undergoing a JT distortion such that the basal plane oxygen atoms are shifted from their (idealized) positions.[29] Such a distortion is termed a Q_2-type JT distortion and alters the Mn-O bond length; the other types are Q_1 (a 'breathing' mode) and Q_3, where the apical oxygen atoms are displaced perpendicular to the basal plan, while oxygen atoms on the basal plane move towards the Mn ion.[28] Unsurprisingly, the changes in Mn-O-Mn bond lengths affect not only the ferromagnetic coupling, but also the metallicity (or lack thereof). Previously, density functional theory calculations have suggested that, for example, the insulating nature of $LaMnO_3$ is strictly due to the occurrence of the Q_2-type JT distortion.[28] Moreover, the directions of the Mn(e_g) orbitals strongly impact the magnetic exchange.[27] Thus, it is apparent, from both theory[16,27,28] and experiment,[31,32] that the types of JT distortions present are critical for determining the transport and magnetic properties of the doped manganites.

The key to understanding these systems, therefore, is to obtain more accurate, local (atomic) chemical and structural information, including the details of the termination, surface reconstruction and the level of segregation of the divalent cation, combined with spatially

resolved studies of functional properties (e.g., electronic structure), and then using the structure and chemical information as inputs to the appropriate first-principles model that can shed light on the physics behind the functionality. Such a level of detail has not been captured by direct experiment and first principles theory before for surfaces of complex oxides; yet these are precisely the studies that are required.

In this article, using a synergistic combination of pulsed laser deposition growth, *in-situ* STM imaging, and first-principles density functional theory (DFT) calculations, we discuss the origin of surface metallic states and insulating behavior[20] of the *A*-site and *B*-site terminated $La_{5/8}Ca_{3/8}MnO_3$ (LCMO) surfaces, respectively. STM and conductive atomic force microscopy (c-AFM) measurements in ultra-high vacuum (UHV) confirm that the surface is metallic for both A-site and B-site terminations for the epitaxially grown films. For the *A*-site terminated surface, we show that the ferromagnetic order of spins and delocalized Mn-*d* states which populate the Fermi energy lead to half-metallic surface states. Interestingly, on the other hand, the *B*-site terminated surface has antiferromagnetic order due to the Ca segregation in the topmost layers of the surface. While the 1x1 *B*-site terminated surface is metallic, the $(\sqrt{2}x\sqrt{2})R45°$ structure is insulating. On the surface, the reduced filling of Mn-*d* orbitals due to 50% Ca segregation, along with Coulombic repulsion between the O-*p* and Mn-*d* states due to Oxygen adatoms, localizes the Mn-*d* orbitals below the Fermi energy, thereby opening up a sizeable band gap (0.8 eV). Our results provide a crucial link between the magnetic order, JT distortion and Ca segregation at LCMO surfaces.

Experimental

LCMO films of 25 unit cell thickness were deposited via pulsed laser deposition at 20mTorr oxygen pressure on etched (001) $SrTiO_3$ substrates, imparting a tensile strain of ~1.2% to the film. Extensive characterization of the surface terminations and growth

conditions are reported elsewhere.[33] After deposition, the film is cooled rapidly and transferred to an SPM chamber at a base pressure $<2.10^{-10}$ Torr for imaging, without exposure of the sample to air. Imaging was achieved via mechanically cut Pt/Ir tips on an Omicron VT-STM/AFM. All STM measurements were carried out at room temperature with V_{tip} = -2V, imaging the empty states in constant-current mode. Typical current setpoints were in the range of 40-100pA.

All calculations are based on density functional theory (DFT) with the Perdew-Burke-Ernzerhof (PBE) parameterization of the generalized gradient approximation[34] (GGA), employing the projector-augmented-plane-wave (PAW) method[35], as implemented in the Vienna Ab initio Simulation Package[36,37] (VASP 5.2). To account for the effect of electronic correlations in these systems, we employed Hubbard *U* parameter on Mn-*d* states in our calculations using the rotationally invariant scheme of Durdev et.al.[38] in which the on-site Coulomb interaction (*U*) and parameter *J* are combined into a single parameter U_{eff} (= *U*-*J*). The U_{eff} for Mn-*d* states was chosen to be 3.9 eV which accurately describes the formation enthalpies of binary and ternary oxides/manganites[39]. We considered a $\sqrt{2}\times\sqrt{2}\times2$ supercell containing 20 atoms that can accommodate all the possible rotations of the MnO_6 octahedra for bulk (La, Ca)MnO_3 for bulk LCMO. The surface geometries are constructed using the symmetric slab model and by multiplying twice the bulk unit cell along *a*,*b* and *c*-axis and the periodic slab images were separated by 15 Å thick vacuum region to avoid spurious Coulombic interactions. Structural optimizations were achieved by allowing the atoms in the unit cell to relax until the Hellmann-Feynman forces on each atomic site were below 5 meV/Å, while simultaneously achieving a total energy convergence of $1e^{-6}$ eV. This convergence was obtained with a 2×2×1 Monkhorst-Pack[40] special *k*-point grid.

Results and Discussion

The large scale STM scan of the LCMO (nominal composition, $La_{5/8}Ca_{3/8}MnO_3$) film is shown in Figure 1(a) and indicates large islands and a mound-like structure. The height distribution is shown in Figure 1(c) and indicates that the islands form roughly half-unit cell step heights suggesting a mixed terminated film with one termination more dominant, in agreement with angle-resolved x-ray photoemission spectroscopy (AR-XPS) reported elsewhere.[33] Note that a line profile along the islands (marked '1' in Fig. 1(a)), and shown in Figure 1(d) again displays half unit-cell step heights. An expanded STM view of the surface is shown in Figure 1(b) illustrates that two distinct reconstructions are present. The islands exhibits a $(\sqrt{2}x\sqrt{2})R45°$ structure, which we identify as the (La,Ca)O-site termination, while the (1x1) structure is the MnO_2-site termination (FFTs inset). As explained in ref.[33], the films studied here have a Ca segregation of ~50% at the top two unit cells (closest to the surface). Figure 1(e,f) further illustrates the atomic arrangements at the (1x1) and $(\sqrt{2}x\sqrt{2})R45°$ surface for both *A*-site ((La,Ca)O) and *B*-site (MnO_2) termination.

To study the surface electronic properties, we turned to scanning tunneling spectroscopy (STS) measurements. Note that STS measurements across a grid of points could not be achieved on our samples due to instability of the tip-sample junction, probably as a result of pickup of oxygen at positive bias.[41] As a result, point spectroscopy mode was utilized and the tip was cleaned via bias pulsing between measurements. The I-V curves from the STS measurement from the areas marked with green and blue circles in Figure 2(a) are shown in Figure 2(b) and are remarkably similar in that both display a clear metallic spectrum, i.e., both terminations show no measurable gap. This result was further confirmed with a local I-V curve taken on the same film via a conductive atomic force microscope tip, plotted in Figure 2(c). Clearly, the non-zero slope through the zero bias point is indicative of surface metallicity in our LCMO films. Note that room temperature macroscopic DC

transport measurements on our films show semiconducting behavior as reported elsewhere.[42] The metallic behavior of the surface was repeatable cross samples grown at different oxygen partial pressures, and has in fact been reported (by c-AFM measurement) previously.[43] The purpose of this work is to explore the surface metallicity in the context of the surface reconstructions present as well as the chemical composition of the surface layers, which are different to the bulk.

To understand the origin of the metallicity, we performed first-principles DFT calculations for both *A* and *B*-site terminated surfaces. The calculations are performed for slabs with (001) surface, which contains an alternating sequence of MnO_2/(La,Ca)O/MnO_2 … up to nine layers along the *c*-axis. We have used symmetrical slabs to avoid the formation of dipole moments, with both the sides having similar terminations e.g. (La,Ca)O for *A*-site terminated slab or MnO_2 for *B*-site terminated slab. Further, both types of surface reconstructions, 1) 1×1 lattice pattern and 2) $(\sqrt{2}\times\sqrt{2})R45°$ were considered for both (*A* and *B*) types of terminations to compare with experimental results (schematic in Fig. 1(e,f)). Before discussing the calculated electronic band structure and the density of states for *A*/*B*-site terminated surfaces, let us first revise the electronic structure of bulk LCMO. Ca doped $LaMnO_3$ exhibits a rich phase diagram in terms of both electronic and magnetic properties depending on the Ca concentration.[25,44] For intermediate concentrations, $0.3<x<0.5$ of Ca in $La_{(1-x)}Ca_xMnO_3$, a phase transition from a high-temperature paramagnetic insulating phase to a low-temperature ferromagnetic (FM) metallic state is observed. Our ground-state (0K) DFT calculations for bulk LCMO (in supplementary[45]) also find ferromagnetically ordered metallic phase at 37.5% Ca concentration and antiferromagnetically ordered insulating phase above 50% concentration of Ca. Thus for ~37.5% Ca doping in the slabs studied here, we considered both the antiferromagnetic (AFM) and ferromagnetic structures for the *A*/*B*-site terminated surface to determine the low temperature ground state. The dopant segregation in

the manganite-based perovskite oxide surfaces has been observed earlier[11,33] and particularly for the films studied here, we expect 50% of Ca concentration in the top layers of the surface.[33] Thus, our model considers 50% of Ca in the topmost layer for the *B*-site terminated surface maintaining overall 37.5% Ca concentration in the LCMO slab.

We begin by exploring the charge density distribution for both *A*-site terminated (i.e., (La,CaO)-terminated (1x1) and $(\sqrt{2}\times\sqrt{2})R45°$ surfaces in Figure 3. The total density maps demonstrates the zig-zag like atomic arrangement corresponding to the orthorhombic structure, inter and intra-planar bonding between Mn-O and La-O along with the absence of charge transfer between the Ca and O atoms. For the (1x1) surface, we observe that the La and Ca atoms in the surface layer are visibly perturbed indicating significant surface reconstruction. The inter-planar separation between the topmost (La,Ca) layer and MnO_2 plane underneath is reduced. Due to a missing MnO_2 sub-lattice on the top, and Q_2 type JT distortions (shown in Fig. 3 (e)), in which the basal plane oxygen atoms are alternately displaced towards and away from the central Mn atom, the ferromagnetic order is stabilized.

Meanwhile, the total charge density distribution for the B-site terminated surface is shown in Figure 4. In the case of *B*-site terminated (1x1) surface, the MnO_6 octahedra are half-open due to the missing oxygen atoms at the apical site. In the $(\sqrt{2}\times\sqrt{2})R45°$ surface, only half of the octahedrons are open, hence the surface cannot fully relax. Instead, a Q_3 type JT distortion sets in, as shown in Fig. 4 (e). In bulk, such a mode would cause increased Coulombic repulsion between the Mn-e_g and the O-p orbitals. At present the resolution of the STM imaging precludes our ability to directly observe the presence of these distortions (phonon modes) at the surface; however, future studies may open the potential to explore this avenue.[46] However, we may proceed on the basis of the electronic structure measured by STS for comparison with the DFT simulations.

The calculated electronic band structure and projected density of states with the projections over La, Ca, Mn and O atoms for *A*-site (La,Ca) terminated surface are shown in Figure 5(a,b), for the 1×1 lattice pattern and (√2×√2)*R*45° surface reconstructions, and for *B*-site (MnO_2) terminated surface in Fig. 5(c,d) for the 1×1 surface and (√2×√2)*R*45° surface reconstruction. As bulk LCMO is a half-metal with ferromagnetic ordering at ~37.5% Ca concentration, similarly, here we observe half-metallic surface states for both the 1×1 and (√2×√2)*R*45° surfaces with ferromagnetic ordering for the A-site terminated surface. Note that the AFM solutions for these two surfaces are observed to be higher in energy compared to the FM ordering. Our results thus confirm the experimental fact that *A*-site terminated LCMO surfaces are metallic irrespective of the type of surface reconstruction. In the bulk, the condensation of a Q2 mode leads to a delocalization of the Mn-eg sub-band, making the system metallic (supplementary Figure S1[45]). But on the surface, there is significant mixing between the e_g and t_{2g} manifold due to the incommensurability between the periodicity imposed by the reconstruction and the wavelength corresponding to the Q2 mode. As a consequence of the mixing, all of the Mn-d orbitals are delocalized and populate the Fermi level leading to metallic nature of A-site terminated surface. The incommensurability is higher for the (√2×√2)R45° reconstructed surface, and hence it shows increased mixing as well as a decreased dispersion of the bands, but exhibits metallic behavior overall. Both the 1×1 lattice pattern and (√2×√2)*R*45° surface reconstruction show similar electronic density of states indicating that the missing oxygen atoms at the surface only affect the number of valence electrons forming metal-oxygen bands. The JT distortion observed in the bulk is also preserved in the surface all the way up to the top-most surface layer, because there are surface Mn-atoms with a complete octahedral environment, as in the bulk. The metallicity at these levels of high doping leads to stabilizing a FM phase as per the Stoner criteria due to an

increase in the density-of-states at the Fermi-level and is consistent with the bulk phase-diagram.

For the *B*-site (MnO_2) terminated surface, we obtain results that differ starkly from the A-site results. The MnO_2 terminated 1x1 surface resembles half-open MnO_6 octahedra with missing apical Oxygen atoms, which are needed to complete the octahedron (refer Figure 1(f)). By placing an oxygen adatom on every other half-open MnO_6 octahedra one constructs $(\sqrt{2}\times\sqrt{2})R45°$ surface. Notably, the AFM order competes with the FM ordering with increasing Ca concentration in the top layer, and is found to be more stable in the case of 50% Ca segregation in the top layers as observed in experiments. The calculated electronic band structure, for both types of surfaces considered, is shown in Figure 5(c,d). Interestingly, we find that while the 1x1 surface with AFM ordering is metallic, the AFM ordered $(\sqrt{2}\times\sqrt{2})R45°$ surface is insulating with a band gap of ~0.8 eV. Furthermore, the bands are significantly less dispersive than those obtained for the A-terminated slabs, indicating significant scatter due to distortions. The tunable metallicity by a surface oxygen overlayer has been earlier confirmed experimentally by Fuchigami *et. al.*,[20] and our calculations agree with these experimental findings, and explain the origin of this gap opening. The calculated AFM band structure (Figure 5(d)) shows that the delocalized Mn-*d* orbital is localized through the Coulombic repulsion with the O-p_z orbital and forms the valence band maximum. Thus as a consequence of Ca segregation, there is a reduction in the electron count on adjacent Mn-atoms, and thus the AFM ordered *B*-site terminated $\sqrt{2}\times\sqrt{2}R45°$ surface is insulating. It should be noted that FM ordered $\sqrt{2}\times\sqrt{2}R45°$ surface is, however, metallic due to the exchange interaction. The contrast between the two termination is most interesting,

considering that the main difference between the A/B-site terminated ($\sqrt{2}\times\sqrt{2}$)*R*45° surfaces in our model is the presence/absence of the A-site atoms (i.e. La/Ca) on the topmost layer. The orbital projected density of states shows that the Fermi level in case of a 1x1 surface is again populated by the delocalized Mn-*d* states and leads to a metallic behavior. In the case of ($\sqrt{2}\times\sqrt{2}$)*R*45° surface, on the other hand, the adsorbed oxygen atom and the absence of A-site atoms play an important role in governing the local electronic structure and leads to insulating behavior. It is worthy to mention that the DFT results mentioned here can reproduce not only our own experimental data, but also data from previous work[20], as well as the bulk properties[44] of this system, which suggests that the Hubbard correction factor used here is indeed appropriate.

Conclusions

The results reported here suggest the possibility for tunable half-metallic surfaces in the manganites, which opens pathways for optimizing devices such as spin valves.[47,48] Moreover, this research, along with our previous work on this system[33] and those of others,[9–12] shows that surface segregation of divalent cations in the doped manganese oxides cannot be neglected when determining the functional properties of the surface (or interface, in the case of oxide heterostructures). Recent density functional theory calculations on prototypical perovskite ferroelectrics by Saidi *et al.*[49] show considerable effects of ionic reconstructions at polar surfaces on the ferroelectric (and electroresistive[50]) properties. Given that manganites such as LCMO and $La_{1-x}Sr_xMnO_3$ are commonly used as bottom electrodes in ferroelectric oxide heterostructures, this study provides a pathway towards control over the interface properties, which can then directly impact the functional property of the grown ferroelectric layer. For example, it has been known that termination dependencies in these heterostructures can give rise to substantial changes in magnitude (and even suppression) of polarization,[51,52] as well dramatically altering the tunneling electroresistance in ferroelectric tunnel junctions.[53] Also, given the propensity for use of manganites in tunnel junctions,[54] these studies confirm the necessity to appropriately characterizing the interface/surface[55] (including the level of segregation) in order to correctly model their properties. These studies confirm the structure-property relations at the atomic scale on the surface of the most commonly studied manganite, LCMO, with *in-situ* STM measurements and appropriate first principles theory, and suggest routes towards surface electronic control by optimizing dopant segregation levels. Specifically, the tunable metallicity and magnetic order depending on the surface reconstruction and composition offer useful control over the device properties in nanoelectronic and spintronic applications.

Contributions

RKV and HD contributed equally to this manuscript.

Conflicts of interest

There are no conflicts to declare

Acknowledgements

The experimental work was supported by the U.S. Department of Energy (DOE), Office of Science (OS), Basic Energy Sciences, Materials Sciences and Engineering Division (RKV, SVK, TM, HNL). DFT work was supported by the OS Early Career Research Program (VRC, HD). Research was conducted at the Center for Nanophase Materials Sciences, which also provided support (APB, PG) and is a DOE OS User Facility. This research used resources of the National Energy Research Scientific Computing Center, a DOE OS User Facility supported by the OS of the U.S. DOE under Contract No. DE-AC02-05CH11231. A.T. acknowledges CICECO-Aveiro Institute of Materials, POCI-01-0145-FEDER-007679 (FCT Ref. UID /CTM /50011/2013), financed by national funds through the FCT/MEC and when appropriate co-financed by FEDER under the PT2020 Partnership Agreement.

References

1 S. Farokhipoor, C. Magén, S. Venkatesan, J. Íñiguez, C. J. M. Daumont, D. Rubi, E. Snoeck, M. Mostovoy, C. de Graaf and A. Müller, *Nature*, 2014, **515**, 379–383.

2 J. A. Bert, B. Kalisky, C. Bell, M. Kim, Y. Hikita, H. Y. Hwang and K. A. Moler, *Nat Phys*, 2011, **7**, 767–771.

3 S. D. Ha and S. Ramanathan, *J. Appl. Phys.*, 2011, **110**, 71101.

4 M. P. Warusawithana, C. Richter, J. A. Mundy, P. Roy, J. Ludwig, S. Paetel, T. Heeg, A. A. Pawlicki, L. F. Kourkoutis, M. Zheng, M. Lee, B. Mulcahy, W. Zander, Y. Zhu, J. Schubert, J. N. Eckstein, D. A. Muller, C. S. Hellberg, J. Mannhart and D. G. Schlom, *Nat Commun*, 2013, **4**.

5 A. M. Haghiri-Gosnet and J. P. Renard, *J. Phys. D. Appl. Phys.*, 2003, **36**, R127.

6 M. B. Salamon and M. Jaime, *Rev. Mod. Phys.*, 2001, **73**, 583.

7 Y. Ogimoto, M. Nakamura, N. Takubo, H. Tamaru, M. Izumi and K. Miyano, *Phys. Rev. B*, 2005, **71**, 60403.

8 M. Rajeswari, R. Shreekala, A. Goyal, S. E. Lofland, S. M. Bhagat, K. Ghosh, R. P. Sharma, R. L. Greene, R. Ramesh and T. Venkatesan, *Appl. Phys. Lett.*, 1998, **73**, 2672–2674.

9 J. Simon, T. Walther, W. Mader, J. Klein, D. Reisinger, L. Alff and R. Gross, *Appl. Phys. Lett.*, 2004, **84**, 3882–3884.

10 T. T. Fister, D. D. Fong, J. A. Eastman, P. M. Baldo, M. J. Highland, P. H. Fuoss, K. R. Balasubramaniam, J. C. Meador and P. A. Salvador, *Appl. Phys. Lett.*, 2008, **93**, 151903–151904.

11 W. Lee, J. W. Han, Y. Chen, Z. Cai and B. Yildiz, *J. Am. Chem. Soc.*, 2013, **135**, 7909–7925.

12 E. J. Moon, P. V Balachandran, B. J. Kirby, D. J. Keavney, R. J. Sichel-Tissot, C. M. Schlepütz, E. Karapetrova, X. M. Cheng, J. M. Rondinelli and S. J. May, *Nano Lett.*, 2014, **14**, 2509–2514.

13 J. Salafranca, R. Yu and E. Dagotto, *Phys. Rev. B*, 2010, **81**, 245122.

14 J. Dvorak, Y. U. Idzerda, S. B. Ogale, S. Shinde, T. Wu, T. Venkatesan, R. Godfrey and R. Ramesh, *J. Appl. Phys.*, 2005, **97**, 10C102.

15 B. Vengalis, A. Maneikis, F. Anisimovas, R. Butkut, L. Dapkus and A. Kindurys, *J. Magn. Magn. Mater.*, 2000, **211**, 35–40.

16 J. M. Rondinelli and N. A. Spaldin, *Adv. Mater.*, 2011, 23, 3363–3381.

17 H. L. Zhuang, P. Ganesh, V. R. Cooper, H. Xu and P. R. C. Kent, *Phys. Rev. B*, 2014, **90**, 64106.

18 A. Lopez-Bezanilla, P. Ganesh and P. B. Littlewood, *Phys. Rev. B*, 2015, **92**, 115112.

19 J. X. Ma, D. T. Gillaspie, E. W. Plummer and J. Shen, *Phys. Rev. Lett.*, 2005, **95**, 237210.

20 K. Fuchigami, Z. Gai, T. Z. Ward, L. F. Yin, P. C. Snijders, E. W. Plummer and J. Shen, *Phys. Rev. Lett.*, 2009, **102**, 66104.

21 T. Chien, N. P. Guisinger and J. W. Freeland, *J. Vac. Sci. & Technol. B*, 2010, **28**, C5A11-C5A13.

22 T. Y. Chien, J. Chakhalian, J. W. Freeland and N. P. Guisinger, *Adv. Funct. Mater.*, 2013, **23**, 2565–2575.

23 T. Ohsawa, R. Shimizu, K. Iwaya and T. Hitosugi, *ACS Nano*, 2014, **8**, 2223–2229.

24 A. Tselev, P. Ganesh, L. Qiao, W. Siemons, Z. Gai, M. D. Biegalski, A. P. Baddorf and S. V Kalinin, *ACS Nano*, 2013, **7**, 4403–4413.

25 J. Y. T. Wei, N.-C. Yeh and R. P. Vasquez, *Phys. Rev. Lett.*, 1997, **79**, 5150–5153.

26 J. Choi, J. Zhang, S.-H. Liou, P. Dowben and E. Plummer, *Phys. Rev. B*, 1999, 59, 13453–13459.

27 H. Meskine, H. König and S. Satpathy, *Phys. Rev. B*, 2001, 64.

28 S. Satpathy, Z. Popović and F. Vukajlović, *Phys. Rev. Lett.*, 1996, 76, 960–963.

29 J. B. Goodenough, *Phys. Rev.*, 1955, **100**, 564–573.

30 P. A. Cox, *Transition metal oxides: an introduction to their electronic structure and properties*, OUP Oxford, 2010, vol. 27.

31 M. N. Iliev, M. V Abrashev, V. N. Popov and V. G. Hadjiev, *Phys. Rev. B*, 2003, **67**, 212301.

32 N. C. Yeh, R. P. Vasquez, D. A. Beam, C. C. Fu, J. Huynh and G. Beach, *J. Phys. Condens. Matter*, 1997, **9**, 3713.

33 A. Tselev, R. K. Vasudevan, A. G. Gianfrancesco, L. Qiao, P. Ganesh, T. L. Meyer, H. N. Lee, M. D. Biegalski, A. P. Baddorf and S. V. Kalinin, *ACS Nano*, 2015, **9**, 4316–4327.

34 J. P. Perdew, K. Burke and M. Ernzerhof, *Phys. Rev. Lett.*, 1996, **77**, 3865.

35 P. E. Blöchl, *Phys. Rev. B*, 1994, **50**, 17953–17979.

36 G. Kresse and J. Furthmüller, *Comput. Mater. Sci.*, 1996, **6**, 15–50.

37 G. Kresse and J. Furthmüller, *Phys. Rev. B*, 1996, **54**, 11169–11186.

38 S. L. Dudarev, G. A. Botton, S. Y. Savrasov, C. J. Humphreys and A. P. Sutton, *Phys. Rev. B*, 1998, **57**, 1505.

39 A. Jain, G. Hautier, S. P. Ong, C. J. Moore, C. C. Fischer, K. A. Persson and G. Ceder, *Phys. Rev. B*, 2011, **84**, 45115.

40 H. J. Monkhorst and J. D. Pack, *Phys. Rev. B*, 1976, **13**, 5188–5192.

41 R. K. Vasudevan, A. Tselev, A. G. Gianfrancesco, A. P. Baddorf and S. V Kalinin, *Appl. Phys. Lett.*, 2015, **106**, 143107.

42 A. Tselev, R. K. Vasudevan, A. G. Gianfrancesco, L. Qiao, T. L. Meyer, H. N. Lee, M. D. Biegalski, A. P. Baddorf and S. V. Kalinin, *Cryst. Growth Des.*, 2016, **16**.

43 S. J. Kelly, Y. Kim, E. Eliseev, A. Morozovska, S. Jesse, M. D. Biegalski, J. F. Mitchell, H. Zheng, J. Aarts, I. Hwang, S. Oh, J. S. Choi, T. Choi, B. H. Park, S. V. Kalinin and P. Maksymovych, *Nanotechnology*, 2014, **25**, 475302.

44 P. Schiffer, A. P. Ramirez, W. Bao and S. W. Cheong, *Phys. Rev. Lett.*, 1995, **75**, 3336.

45 See Supplemental Material at [URL will be inserted by publisher] for results of bulk DFT calculations

46 W. Lin, Q. Li, B. C. Sales, S. Jesse, A. S. Sefat, S. V. Kalinin and M. Pan, *ACS Nano*, 2013, **7**, 2634–2641.

47 Y. W. Yin, J. D. Burton, Y.-M. Kim, a Y. Borisevich, S. J. Pennycook, S. M. Yang, T. W. Noh, A. Gruverman, X. G. Li, E. Y. Tsymbal and Q. Li, *Nat. Mater.*, 2013, **12**, 1–6.

48 D. Pantel, S. Goetze, D. Hesse and M. Alexe, *Nat. Mater.*, 2012, **11**, 289–293.

49 W. A. Saidi, J. M. P. Martirez and A. M. Rappe, *Nano Lett.*, 2014, **14**, 6711–6717.

50 G. Radaelli, D. Gutiérrez, F. Sánchez, R. Bertacco, M. Stengel and J. Fontcuberta, *Adv. Mater.*, 2015, **27**, 2602–2607.

51 Y.-M. Kim, A. Kumar, A. Hatt, A. N. Morozovska, A. Tselev, M. D. Biegalski, I. Ivanov, E. A. Eliseev, S. J. Pennycook, J. M. Rondinelli, S. V Kalinin and A. Y. Borisevich, *Adv. Mater.*, 2013, **25**, 2497–2504.

52 Y.-M. Kim, A. Morozovska, E. Eliseev, M. P. Oxley, R. Mishra, S. M. Selbach, T. Grande, S. T. Pantelides, S. V Kalinin and A. Y. Borisevich, *Nat. Mater.*, 2014, **13**, 1019–1025.

53 H. Yamada, A. Tsurumaki-Fukuchi, M. Kobayashi, T. Nagai, Y. Toyosaki, H. Kumigashira and A. Sawa, *Adv. Funct. Mater.*, 2015, **25**, 2708–2714.

54 V. Garcia and M. Bibes, *Nat. Commun.*, 2014, **5**, 4289.

55 A. Tselev, R. K. Vasudevan, S. V Kalinin and A. P. Baddorf, *Appl. Phys. Lett.*, 2014, **105**, 101602.

Figure Captions

Figure 1: (a) Large scale STM topography of the surface of the LCMO film. **(b)** Atomically resolved image of the surface, showing two distinct terminations and two different reconstructions. Fast Fourier Transform (FFT) images of the white boxed regions in (b), inset highlights the two different lattice structures. Scale bar in inset, $4nm^{-1}$ **(c)** Height distribution showing half unit cells intervals. **(d)** Line profile of segment '1' in (a), confirming half-unit cell steps. Schematic view of (1x1) and ($\sqrt{2}$x$\sqrt{2}$)*R*45° surfaces for **(e)** (La,Ca)O and **(f)** MnO_2 termination. Black lines highlight the unit cell for each type of surface. Green atoms are La/Ca, red atoms are oxygen, and purple atoms are Mn.

Figure 2: (a) STM topography of area where STS was performed. **(b)** I-V spectra taken at points indicated by the blue and green circles in (a), corresponding to the two distinct terminations. **(c)** I-V taken by an AFM tip on the same film, showing metallic behavior.

Figure 3: Total electron density distribution for *A*-site terminated LCMO (001) 1x1 surface with **a)**top and **b)**side view. For the $\sqrt{2}\times\sqrt{2}$R45° surface, **c)** shows top and **d)** shows the side view of the surface. The electron density of the isosurface corresponds to the value of 0.039 $e/Å^3$. The isosurface sections are shown in blue, while the La, Ca, Mn, and O atoms are shown in green, blue, magenta and red, respectively.

Figure 4: Total electron density distribution for *B*-site terminated LCMO (001) 1x1 surface with **a:**top and **b)**side view. For the ($\sqrt{2}\times\sqrt{2}$)R45° surface, c**)** shows top and d**)** shows the side view of the surface. The electron density of the isosurface corresponds to the value of 0.039 $e/Å^3$. The isosurface sections are shown in blue, while the La, Ca, Mn, and O atoms are shown in green, blue, magenta and red, respectively.

Figure 5: Electronic band structure and orbital projected density of states (PDOS) corresponding to *A*-site (La,Ca, O) terminated $La_{0.625}Ca_{0.375}MnO_3$ (001) **(a)** 1x1 and **(b)** ($\sqrt{2}\times\sqrt{2}$)*R*45° surface, and to *B*-site (MnO_2) terminated $La_{0.625}Ca_{0.375}MnO_3$ (001) **(c)** 1x1 and **(d)** ($\sqrt{2}\times\sqrt{2}$)*R*45° surface. The Mn-e_g, Mn-t_{2g} and O-*p* states contributing to the valence band maximum and the conduction band minimum are shown in red, green and blue color, respectively. In the PDOS, only the states contributing to the spin up channel are shown for clarity.

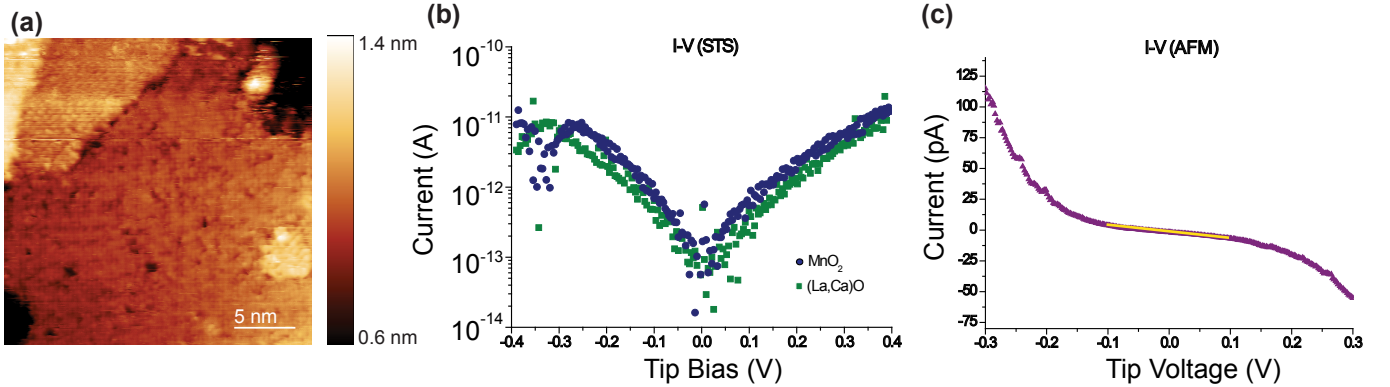
(a)
1.4 nm
0.6 nm
5 nm
(b)
I-V (STS)
Current (A)
Tip Bias (V)
MnO2
(La,Ca)O
(c)
I-V (AFM)
Current (pA)
Tip Voltage (V)

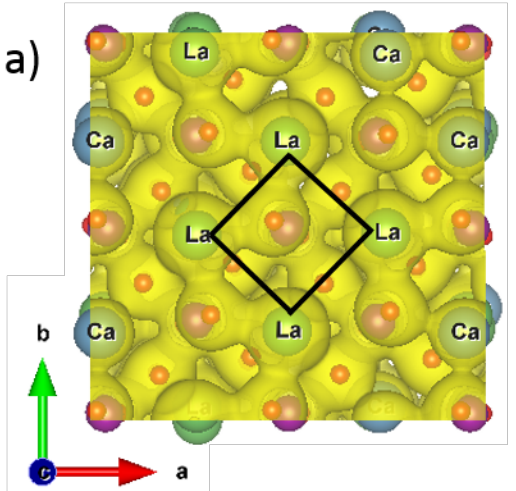

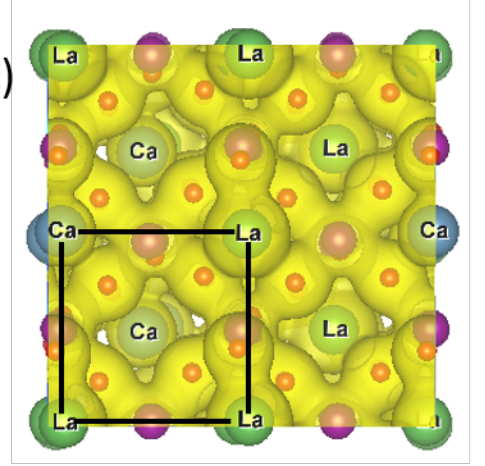

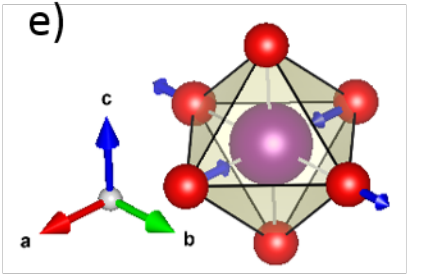

Q_2 type Jahn-Teller distortion

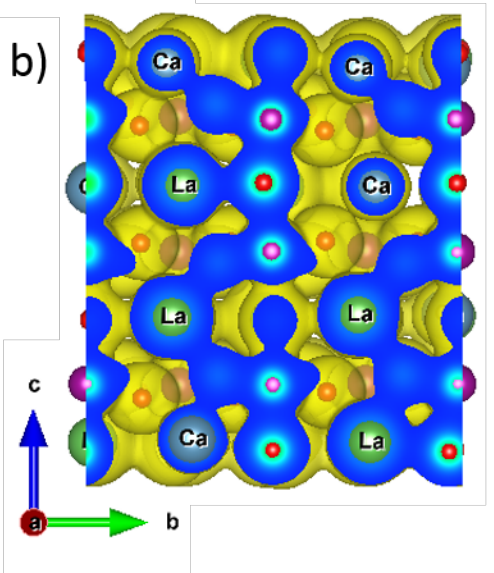

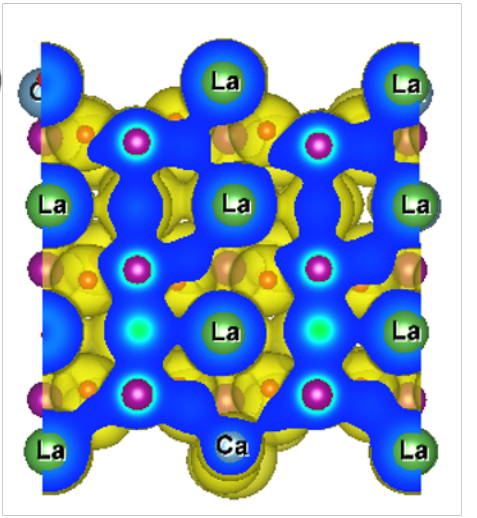

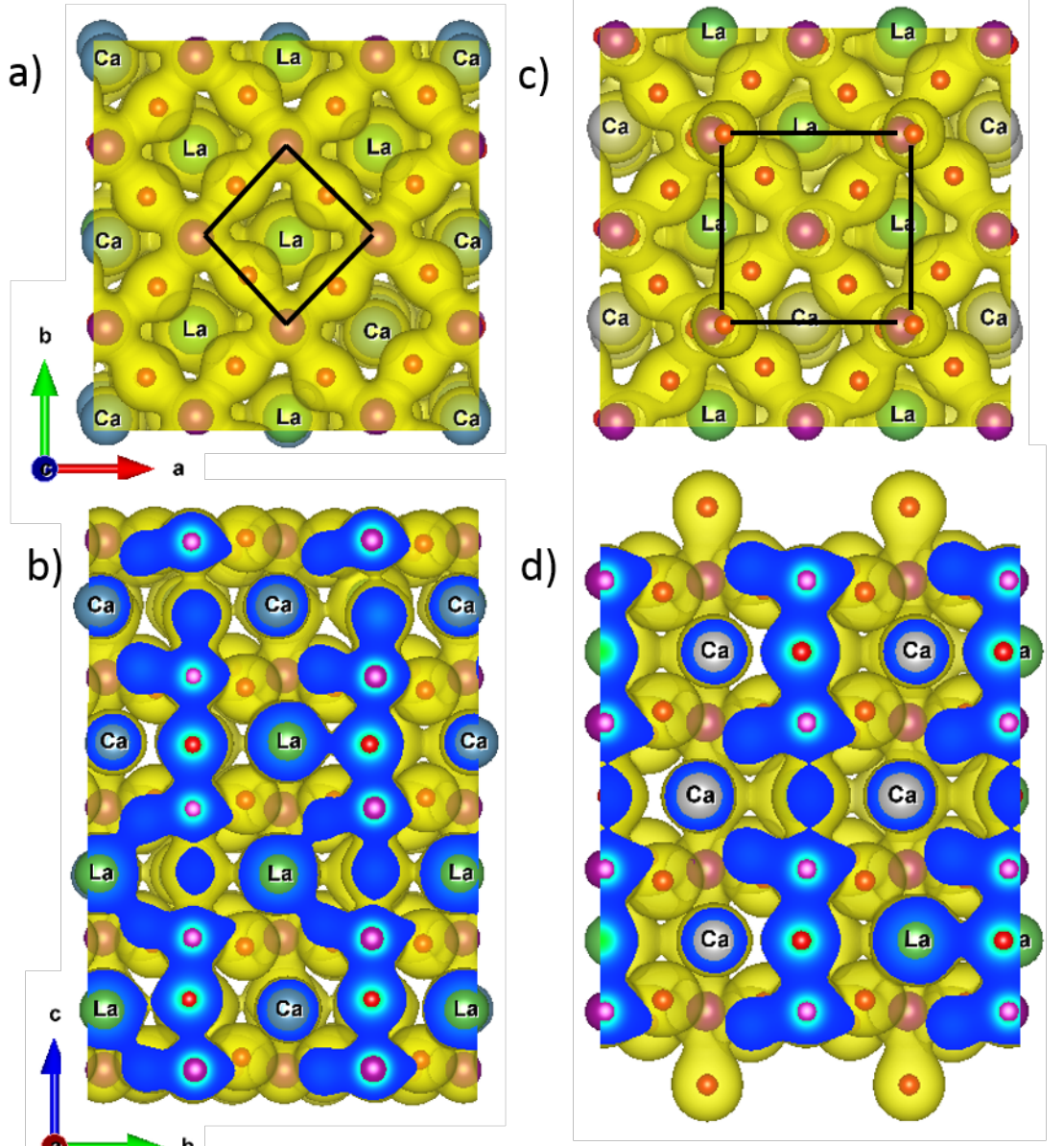

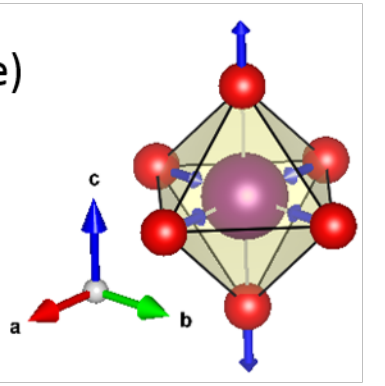

Q_3 type Jahn-Teller distortion

(a) (La,Ca)O terminated (1x1)

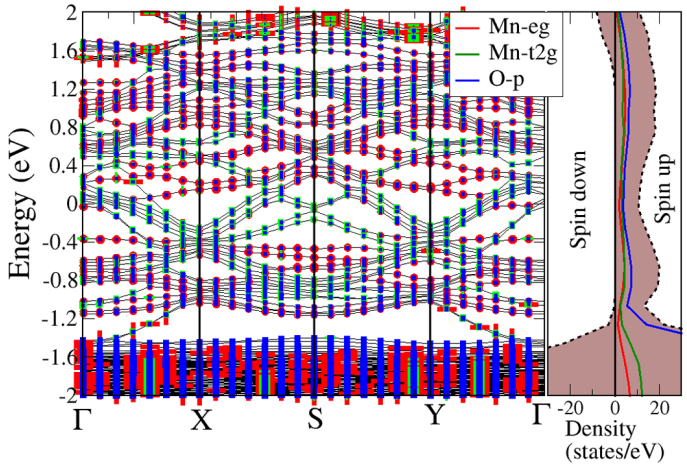

(b) (La,Ca)O terminated (√2×√2)*R*45°

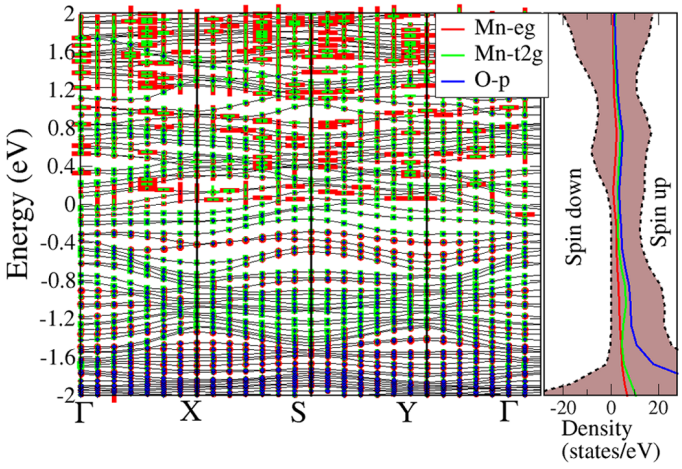

(c) MnO_2 terminated (1x1)

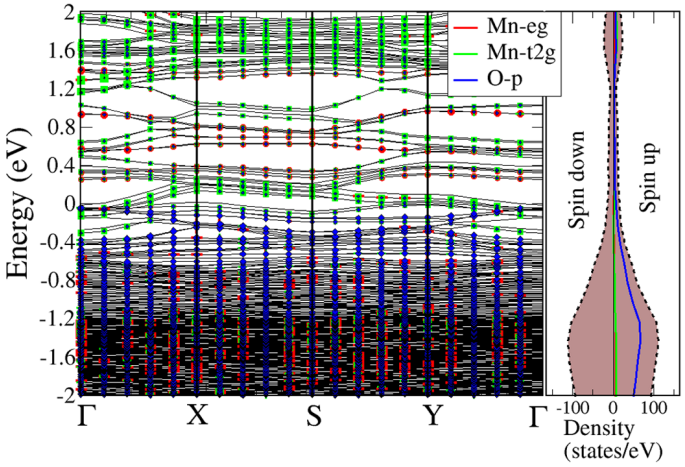

(d) MnO_2 terminated (√2×√2)*R*45°